



HAL
open science

Probing the dynamics of the photo-induced decarboxylation of neutral and ionic pyruvic acid

M. Jarraya, A. Bellili, L. Barreau, D. Cubaynes, G. A. Garcia, L. Poisson, M. Hochlaf

► **To cite this version:**

M. Jarraya, A. Bellili, L. Barreau, D. Cubaynes, G. A. Garcia, et al.. Probing the dynamics of the photo-induced decarboxylation of neutral and ionic pyruvic acid. *Faraday Discussions*, 2022, 238, pp.266-294. 10.1039/D2FD00023G . hal-04234713

HAL Id: hal-04234713

<https://hal.science/hal-04234713>

Submitted on 10 Oct 2023

HAL is a multi-disciplinary open access archive for the deposit and dissemination of scientific research documents, whether they are published or not. The documents may come from teaching and research institutions in France or abroad, or from public or private research centers.

L'archive ouverte pluridisciplinaire **HAL**, est destinée au dépôt et à la diffusion de documents scientifiques de niveau recherche, publiés ou non, émanant des établissements d'enseignement et de recherche français ou étrangers, des laboratoires publics ou privés.

Probing the dynamics of the photo-induced decarboxylation of neutral and ionic pyruvic acid

M. Jarraya^{1,2}, A. Bellili³, L. Barreau⁴, D. Cubaynes⁴, G. A. Garcia⁵, L. Poisson^{4,*}, M. Hochlaf^{1,*}

¹ U. Gustave Eiffel, COSYS/LISIS, 5 Bd Descartes 77454, Champs-sur-Marne, France.

² Laboratoire de Spectroscopie Atomique, Moléculaire et Applications – LSAMA, Université de Tunis El Manar, Tunis, Tunisia.

³ U. Houari Boumediene des Sciences et Technologies, LTMM, Algiers, Algeria.

⁴ Université Paris-Saclay, CNRS, Institut des Sciences Moléculaires d'Orsay, 91405, Orsay, France.

⁵ Synchrotron SOLEIL, L'orme des Merisiers, Saint-Aubin - BP 48 - 91192 Gif-sur-Yvette Cedex, France

Authors for correspondance :

*emails: lionel.poisson@universite-paris-saclay.fr (L.P.); majdi.hochlaf@univ-eiffel.fr (M.H.)

Abstract

The dynamics of the electronically excited pyruvic acid (PA) and of its unimolecular decomposition upon single photon ionization are investigated by means of a table top fs laser and VUV synchrotron radiation. The latter is coupled with photo-ion/photo-electron coincidence acquisition devices that allow the identification of the ionic products coming from state-to-state fragmentation upon ionisation. The fs-based setup provides time-resolved mass spectra with 266 nm (= 4.661 eV) excitation and 800 nm multiphoton probe. For interpretation, we carried out theoretical computations using a composite scheme combining density functional theory full molecular geometry optimisation and post-Hartree-Fock corrections inclusion. We therefore determined the neutral and ionic species formed during these experiments and the corresponding dissociation channels. Although several PA isomers are found, we show that solely the most stable isomer of PA (i.e. Tc) is present in the molecular beam prior to ionisation. We determined its adiabatic ionisation energy (AIE = 10.031 ± 0.005 eV). The fragmentation of the Tc⁺ ion occurs ~0.4 eV above threshold and it is dominated by the CC bond breaking channel forming HOCO fragment in conjunction with CH₃CO⁺ ion. The CO₂ decarboxylation of Tc⁺ channels have a minor contribution although they are more favourable thermodynamically. These findings are in contrast with the dominance of decarboxylation while fragmenting Tc populated in the S₁-S₃ states. For explanation, we invoke an indirect process populating first a short lived autoionising neutral state located in energy at the HOCO + CH₃CO⁺ dissociation limit. Later on, fragmentation occurs followed by autoionisation. On the other hand, the fs-based experiment does not reveal any appreciable dynamics for Tc isomer of PA after a 266 nm excitation because of non-favourable Franck-Condon factors at this energy. In sum, our work highlights the importance of the couplings between the parent ion vibrational modes and the dissociative channels in the vicinity of the loss ionic fragmentation thresholds.

I. Introduction

Pyruvic acid ($\text{CH}_3\text{CO-COOH}$, PA) is important for life chemistry. For instance, it is an important molecule for metabolism as it is involved in the energy production from glucose, where its anion, formed by sugar glycolysis, is further used with nicotinamide adenine dinucleotide (NAD^+) to generate Acetyl-CoEnzyme A and NADH through the loss of CO_2 .¹ Besides, PA is involved in atmospheric chemistry, where it is identified as part of atmospheric aerosols, rains and in the gas phase.^{2,3} It is emitted directly by animals and plants and produced by the oxidation of Volatile Organic Compounds.⁴ It plays a key role as intermediate in keto-acid reactions, as product of oxidation of cresols and of isoprene and of secondary organic aerosols (SOA).^{2,3,5,6} It is also formed after reactions between OH and hydrated methylglyoxal and between O_3 and methyl vinyl ketone.^{7,8} Moreover, although PA has not yet been reported in the interstellar medium, its possible formation in cold molecular clouds and star-forming regions was recently raised by Kaiser and co-workers, who showed that PA can be efficiently produced through the cosmic rays driven barrier less reactions between HOCO and CH_3CO radicals in ices of acetaldehyde and carbon dioxide miming interstellar conditions.⁹ It should be noted that the search of PA in astrophysical media is a very active field. This is based on the numerous available accurate data for this species including its rotational and vibrational spectroscopic parameters, where several isomers, conformers and tautomers were investigated. Experimentally, these data are acquired through the analysis of the corresponding microwave (μw) and infrared (IR) spectra of these species either isolated or trapped in cold matrices.^{10,11,12,13,14,15,16,17,18,19} These works are complemented by theoretical computations at density functional theory (DFT) and post Hartree-Fock configuration interactions levels.^{16,19,20,21,22,23,24,25,26}

The electronic structure of PA is known through the analysis of its UV-VIS spectrum and theoretical computations.^{27,28,29,30} These works located the adiabatic energy for the S_0 - S_1 transition at 3.31 eV and the vertical excitation energies of the S_0 - S_2 and the S_0 - S_3 transitions at 5.60 eV and 7.00 eV, respectively. Also, previous studies showed that electronically excited PA undergoes a complex chemistry. Indeed, the photochemistry of isolated gas phase PA or in atmospheric conditions, has a peculiar reaction dynamics dominated by photo-dissociation forming CO_2 and other fragments.^{24,27,29,31,32,33,34,35,36,37,38,39} In the troposphere, solar radiation photolysis of PA is, for instance, the dominant destruction process of this acid rather than its reactions with free radicals such as OH.⁴⁰ Experimentally, the photochemistry of PA has been studied either by photon excitation at $\lambda \sim 320$ -380 nm (= 3.26 - 3.87 eV) or at $\lambda \sim 193$ nm (= 6.42 eV). At $\lambda \sim 320$ -380 nm, the photon absorption populates predominantly the S_1 state, which evolves mainly by the ejection of a CO_2 molecule and the formation of methylhydroxycarbene radical, which isomerizes to give acetaldehyde.^{24,27,30,35} Therefore, it was suggested that the primary process in the photolysis is a concerted hydrogen transfer and carbon-carbon bond cleavage to produce CO_2 and the methylhydroxycarbene radical, with the latter then rearranging to give CH_3CHO . This is confirmed theoretically.^{31,34,37} For instance, Chang et al.³¹ investigated the mechanistic photodecarboxylation of PA in the S_0 , T_1 , and S_1 states. Through the analysis of the potential

energy surfaces of these electronic states generated at the complete active space self-consistent field and its multi-state second order perturbation methods, these authors showed that the triplet state is located slightly below S_1 at the equilibrium geometry of S_0 and that this molecular system is characterized by a three-state intersection, where a S_0/S_1 conical intersection and a S_1/T_1 and S_0/T_1 intersystem crossings are located at the same nuclear configuration. This potential energy region is crucial for the photodecarboxylation and it is reached after tautomerism on the S_1 state, where the hydrogen transfer occurs at least partially by tunnelling, in competition with the S_1-T_1 spin-orbit conversion at their crossing. Moreover, it was shown that a comparable Norrish type I reaction takes place in the T_1 state, which forms the ground-state products of CH_3CO and $HOCO$. This channel is minor and accounts for < 3% branching ratio (BR). Besides, experimental and theoretical PA conformer-specific photolysis results revealed that PA most stable conformer dominates the gas-phase PA photolysis.²⁴ At shorter wavelengths ($\lambda \sim 193$ nm), the S_3 state is populated and the dissociation on this electronic state is fast. The subsequent fragmentation leads to CO_2 , CO , H , OH , HCO , $HOCO$, CH_2CO , CH_3CO , and CH_3 in addition to minor products such as acetaldehyde and vinyl alcohol photoproducts and HCO , H_2CO , and CH_4 products arising from their unimolecular dissociation.^{41,42} At this excitation energy, the decarboxylation terminating in CO_2 + other primary products remains a dominant channel, whereas its BR is reduced to $\sim 50\%$ while the Norrish type I dissociation BR is increased to $\sim 30\%$ and the O-H and C-H bond breaking reactions generating the H atom accounts for $\sim 10\%$.⁴² The OH formation involves internal conversion and intersystem crossing from the initially populated S_3 state to T_1 state followed by the dissociation from T_1 . This is supported by ab initio calculations on PA excited electronic states as carried out at the configuration interaction with single electronic excitation level in conjunction with the 6-311G(d,p) basis set.⁴¹ Nevertheless, the other photoproducts are found to be formed by rapid three-body fragmentation processes.

Although the neutral PA molecule was largely treated in the literature, this is not the case for its cation despite its likely relevance in an astrophysical context, where cosmic radiations lead to ionisation and ionisation induced fragmentations that reduced the possibilities for space regions where the neutral molecules can be formed and detected. Back in 1975, McGlynn and Meeks⁴³ recorded the photoelectron spectrum (PES) of PA. They determined the adiabatic ionisation energy (AIE) of PA as 10.1 ± 0.1 eV as the transition populating the D_0 cationic state from the neutral. The vertical ionization energies (VIEs) of D_0 , D_1 , D_2 , D_3 , D_4 , D_5 , D_6 and D_7 cationic states are located at 10.42, 12.31, 12.42, 13.79, 15.16, 15.64, 16.63 and 17.59, all values in eV. Based on semi-empirical Complete Neglect of Differential Overlap (CNDO) computations, they tentatively assigned the population of the corresponding PES bands to the ejection of an electron from the n_+ , π_+ , n_- , π_- and π_+ outermost molecular orbitals (MOs). In 1976, Lossing and Traeger⁴⁴ showed that PA cation decomposes to give an ionic fragment with m/z 44 where an appearance energy (AE) > 10.4 eV was measured using energy-selected electrons. Instead, an AE of 10.7 ± 0.2 eV was determined by Terlouw et al.,⁴⁵ in fair agreement with previous value. In 1991, Holmes et al.⁴⁶ determined an AE of 10.28 eV for the $PA \rightarrow CHO_2^+ + C_2H_3O$ fragmentation. Besides, it

is worth citing the recent work by Grygoryeva et al.⁴⁷ who studied isolated $(PA)_n$ clusters and clusters deposited on large water clusters (ice nanoparticles) $(PA)_n(H_2O)_m$, where they followed their photochemistry after either 70 eV electron impact ionization or 193 nm UV photoionization and showed that they exhibit a different chemistry when compared to isolated gas phase PA cations.

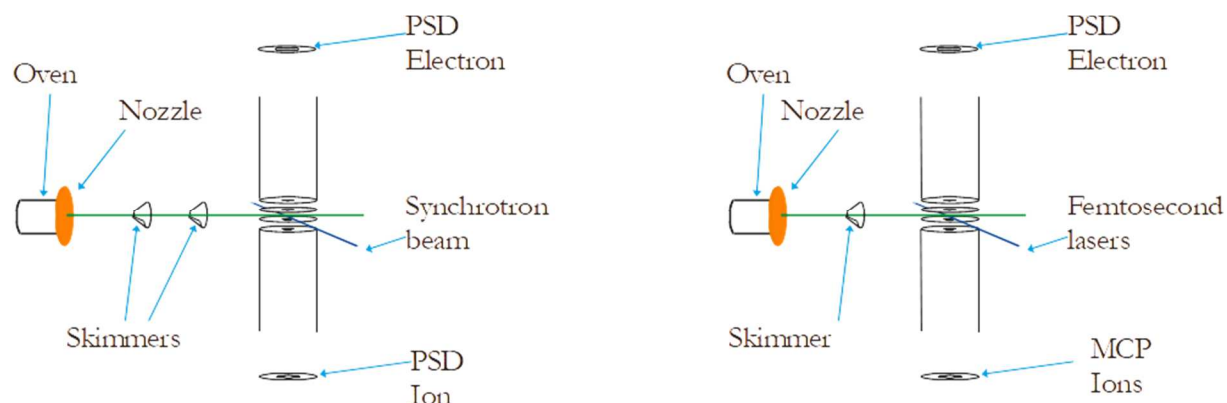


Figure 1: left: Scheme of the experimental setup at Synchrotron SOLEIL, on beamline DESIRS, mounted with the i^2 PEPICO spectrometer DELICIOUS3; (Right) Scheme of the TR-MS experimental setup located at Université Paris-Saclay/ ISMO.

Here, we present an experimental investigation of the dynamics of the photo-induced decarboxylation of neutral PA at short timescales and PA unimolecular fragmentation dynamics upon photoionization, with a special focus on the CO_2 emission channels. These experiments are performed using the VUV DESIRS beamline at the synchrotron SOLEIL⁴⁸ and using a table top fs laser coupled with a NOPA (Figure 1). Time resolved relaxation dynamics of the first excited state will be shown. The identification of the products is done using Velocity Map Imaging (VMI) based coincidence detectors. For the PA cation, we aim at identifying all the fragmentation channels appearing from the AIE ($= 10.1 \pm 0.1$ eV) up to 12.5 eV with respect to the neutral ground state. Ion recoil energies analyses allowed us to discriminate fragmentation pathways and disentangle the contribution of PA monomers from those issued from PA clusters decomposition. These experimental studies are complemented by advanced theoretical computations on the electronic structure of the monomer, either neutral or ionized and on the ionic fragmentation channels. For instance, we mapped the corresponding multidimensional potential energy surfaces in the Franck-Condon region accessed from PA ground state, close to the dissociation asymptotes and along the intramolecular isomerization and fragmentation pathways. Thus, we identify the main reaction pathways mandatory for the in-depth interpretation of the experimental data.^{49,50,51,52}

II. Methodologies

a. VUV single photon ionisation

The VUV single photon ionisation of PA was performed at the DESIRS beamline of the French synchrotron SOLEIL.⁵³ Briefly, the light is produced by an electromagnetic undulator and the high

harmonics removed via a gas filter filled with Ar before being dispersed by a monochromator equipped with a 200 grooves/mm normal incidence grating, which was set to deliver a photon energy resolution of 0.72 Å. The energy scale was absolutely calibrated to a precision of 2 meV using the 5s and 5s' Ar absorption lines from the gas filter.

PA was purchased from Sigma-Aldrich with a purity > 98%. No further purification was done. This sample was placed into an in-vacuum oven and kept at room temperature (body/nozzle). A molecular jet-cooled PA is prepared using the PA vapour after expansion through a 100 µm pinhole using 0.5 bars of He as carrier gas and going through two consecutive skimmers (1 mm and 2 mm diameter) before being ionized by the VUV light. The emitted photoelectrons and photoions were recorded using the double imaging photoelectron-photoion coincidence (i²PEPICO) DELICIOUS3 spectrometer,⁵⁴ which is composed of a VMI electron analyzer⁵⁵ and a photoion momentum imager operated in coincidence, so that the photoelectron images can be tagged by the ion mass and translational energy (see Figure 1-left). The latter allows the separation of direct and dissociative ionization processes for a given mass (critical to avoid cluster fragmentation), and a much better estimation of the appearance energy and barrier height of a given fragmentation channel. At each photon energy, the ion kinetic energy release distribution (KERD) is measured simultaneously.

Ionization processes at play are also monitored by applying the slow photoelectron spectroscopy (SPES) approach⁵⁶ that allows to elucidate the ionization dynamics of autoionizing states.⁵⁷ Shortly, for each mass of interest, the corresponding VMI electron images are inverted by mean of the pBASEX method⁵⁸ with its improved version for low signal.⁵⁹ The method furnishes both the photoelectron energy distribution that generates the collected image, and anisotropy distribution provided that a single photon ionization by a linear polarized light, in the plane of the detector, is in action.

The SPES approach consists in projecting the energy of a band to its expected apparition threshold, and averaging the result of each projection when tuning the photon energy. The main parameter for an SPES spectrum is the maximum kinetic energy of photoelectrons considered for the projection. In the following, we will focus on SPES limited to 50 meV or 800 meV kinetic energy photoelectrons. Hereafter, the resulting spectra will be called "P0" when applied to the total energy distribution. Besides and since non-zero energy photoelectrons are considered, it is also possible to provide information in the anisotropy of this emerging band, averaged on the energy range selected for the SPES spectrum. The previous procedure is applied to the anisotropy distribution matrix, which is the product of "P0" by β_2 (known as the anisotropy parameter). In the following, the resulting spectrum is denoted "P2".

b. fs-spectroscopy

The femtosecond relaxation dynamics of PA at 266 nm (= 4.661 eV) was investigated using time resolved mass spectrometry (TR-MS) experiment. Briefly, a Coherent Legend Elite laser providing 35 fs, 800 nm, 3 kHz pulses with a maximum energy of 4.5 mJ per pulse is used for the pump and probe

scheme. For the current experiment, a total of 2.5 mJ per pulse is used, with 1 mJ being used as the 800 nm (=1.5498 eV) probe pulse. The remaining 1.5 mJ is frequency doubled and mixed to provide 160 μ J at 266 nm used as the pump pulse for the excitation of PA. The relative delay between the pump and the probe pulses is controlled by a delay-line.

The experimental molecular beam and Time-Of-Flight (TOF) ion spectrometer setup were described previously.⁶⁰ Here, the source was adapted to 3 kHz repetition rate laser by using a continuous supersonic expansion with a 100 μ m nozzle. The PA sample was introduced in a flask in which 1 bar of helium was bubbling before the expansion. The laser interaction region is separated from the source by a 1 mm skimmer (see Figure 1-right). Only TR-MS is reported here because of the presence of a significant amount of multimers in the molecular beam that prevents the measurement of photoelectron spectra without coincidence, as done with the synchrotron experiment.

The UV pump and IR probe pulses are both focused into the interaction region of the TOF mass spectrometer where they excite and ionize a molecular beam of PA, their intensity being tuned by moving the lens toward the propagation axis. The multiphoton 800 nm probe ionizes the excited PA molecules in a [1 + ≥ 4] scheme. Afterwards, the emitted ions are extracted in the TOF mass spectrometer, whose resolution is 465 at m/z 88. The signal issued from the anode placed behind the microchannel plates is collected with an oscilloscope and averaged for 5000 laser shots at each time delay. The experiments are reproduced at least 3 times. All data presented are corrected for the sum of the pump-alone and probe-alone signal.

c. Theoretical computations

We started our computations by determining the equilibrium structures of neutral and ionic PA isomers and the fragments of PA^+ using the density functional PBE0⁶¹ as implemented in GAUSSIAN 16,⁶² where the atoms are described using the aug-cc-pVDZ basis set.^{63,64} These complete geometric optimizations were carried out in the point group C_1 . The minimal character of these stationary points is checked after calculations of harmonic frequencies (all frequencies are positive).

For more accurate energetics, we adopted a PBE0/aug-cc-pVDZ (opt)//(R)CCSD(T)-F12(b)/cc-pVTZ-F12 (+ $\Delta CV + \Delta SR + \Delta ZPVE$) composite scheme.⁴⁹ These computations consist of a series of single point computations on the PBE0/aug-cc-pVDZ optimized structures using post Hartree-Fock methodologies as implemented in MOLPRO 2015.⁶⁵ We also consider the ΔCV (i.e. the core-valence), the ΔSR (i.e. the scalar relativistic) and the $\Delta ZPVE$ (i.e. the zero-point vibrational energy) corrections. For instance, we carried out single point calculations using the coupled cluster explicitly correlated with single, double and perturbative treatment of triple excitations ((R)CCSD(T)-F12) (approximation b),^{66,67,68,69} where the atoms are described with the cc-pVTZ-F12 basis set together with the corresponding resolutions of the identity and density fittings functions.^{70,71} ΔCV is evaluated as the difference between (R)CCSD(T)/cc-pwCVTZ^{72,73} energies with and without considering core electron correlation. The ΔSR

scalar relativistic correction is deduced as the difference between (R)CCSD(T)/cc-pVTZ-DK^{74,75,76} and (R)CCSD(T)/cc-pVTZ energies. Δ ZPVE is obtained at the PBE0/aug-cc-pVDZ level. In a series of previous benchmarks and comparisons with experimental results, we have shown that the presently adopted composite scheme allows the accurate derivation of adiabatic ionization energies and of appearance energies of small and medium-sized molecular systems (within ± 0.005 eV).^{50,51,52}

In addition to the electronic ground states investigations, we carried out electronic calculations of the electronic excited states in the C_s point group. We considered the lowest doublet states of the cation of the most stable form of PA. These calculations are done at the equilibrium geometry of the corresponding neutral species using the state-averaged Complete Active Space Self Consistent Field (SA-CASSCF) approach^{77,78} followed by the explicitly correlated, internally contracted Multi Reference Configuration Interaction (MRCI-F12) technique^{79,80,81} as implemented in MOLPRO 2015. At CASSCF, the active space was constructed by considering the 16 a' - 22 a'' , 2 a'' and 7 a'' MOs as active. The core orbitals and first valence orbitals (up to 15 a' and 1 a'') were kept as closed orbitals. At MRCI-F12, all configurations with coefficients greater than 0.05 in the CI expansion of the CASSCF wave functions were used as a reference. Per C_s symmetry, four doublet states were requested. Atoms have been described using the aug-cc-pVDZ basis set. The accuracy of the relative energies of the electronic states computed at this level of theory should be 0.05 eV.⁴⁹

III. Results and discussion

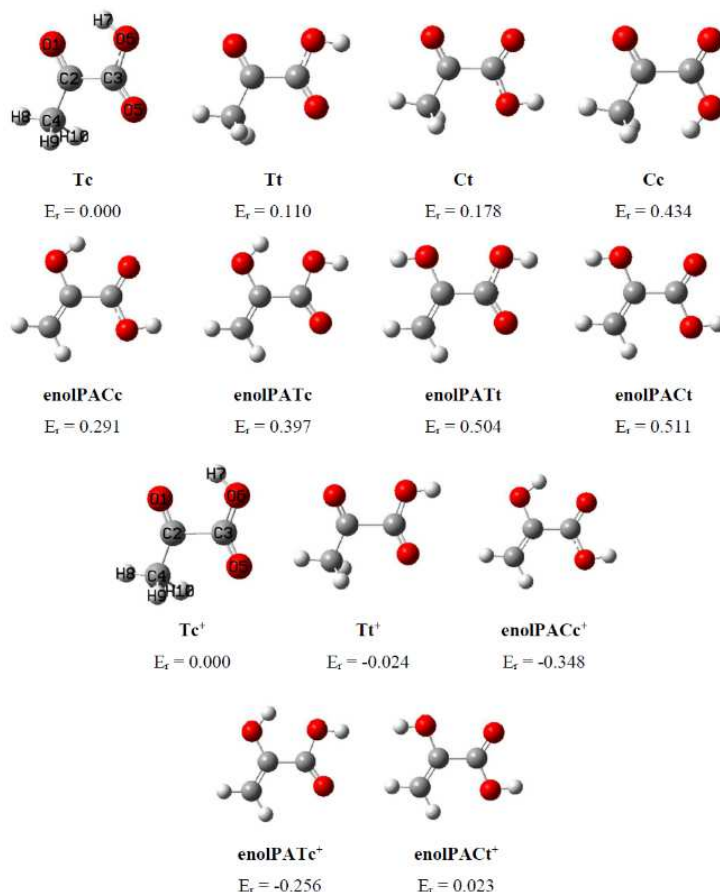


Figure 2: Stable forms of pyruvic acid and of its cation found in the present work. We give their denomination used and their relative energies (E_r in eV), as computed at the PBE0/aug-cc-pVDZ (opt) // (R)CCSD(T)-F12 /cc-pVTZ-F12 + Δ CV+ Δ SR+ Δ ZPVE (SP) level, with respect to the Tc conformer for neutrals and with respect to the Tc⁺ isomer for cations. Cf. Tables S1-S3 of the supplementary material for more details. For Tc and Tc⁺, we give the numbering of the atoms as used in the present study.

PA neutral species were investigated previously using DFT approaches or by CCSD(T) or CCSD(T)-F12 techniques in conjunction with large basis sets, some of them extrapolated to the complete basis set limit (CBS) targeting the determination of accurate rotational and vibrational data of PA conformers and tautomers to help their identification in atmospheric and astrophysical media.^{16,19,20,21,22,23,24,25,26,34} These works characterised 4 keto-acid forms (denoted Tc, Tt, Ct, Cc) and 4 enol-acid tautomers (denoted enolPACc, enolPATc, enolPATt, enolPACt). Here, we carried out PBE0/aug-cc-pVDZ optimisations which confirm the minimal structure of these isomers. They are displayed in Figure 2. Afterwards, we carried out CCSD(T)-F12 /cc-pVTZ-F12 + Δ CV+ Δ SR+ Δ ZPVE (SP) single point computations at the corresponding PBE0/aug-cc-pVDZ optimised structure to deduce accurately the relative energies of these isomers. As previously established, Tc is the most stable form followed up in energy by Tt and then Ct at 0.110 eV and 0.178 eV, respectively. The other forms are lying > 0.2 eV

with respect to Tc. These relative energies and ordering are consistent with those previously computed. In particular, they differ by less than 0.002 eV from the relative energies computed by Barone et al.²¹ for the keto-acid species using the B2PLYP/aug-cc-pVTZ//CCSD(T)/CBS+CV composite scheme.

Using the neutral minimal structures as a starting point, we searched for PA cationic stable isomers. Upon full optimisations, we found only 5 stable forms in the ground potential energy surface of PA⁺. They are displayed in Figure 2, where they are denoted as Tc⁺, Tt⁺, enolPACc⁺, enolPATc⁺ and enolPACT⁺. The two former ones are keto-acid compounds similar to Tc and Tt neutrals and the three others are singly charged ions of enolPACc, enolPATc and enolPACT. At the PBE0/aug-cc-pVDZ (opt) // RCCSD(T)-F12 /cc-pVTZ-F12 + Δ CV+ Δ SR+ Δ ZPVE (SP) level, the most stable cationic form is enolPACc⁺, followed in energy by enolPATc⁺, Tt⁺, Tc⁺ and enolPACT⁺ at 0.092, 0.324, 0.348 and 0.371 eV respectively.

Barone et al.²¹ computed the following potential barriers: Tc \rightarrow Tt : 0.602 eV and Tt \rightarrow Ct : 0.224 eV. For the methyl internal rotation, potential barriers of 0.042 eV, 0.049 eV, 0.067 eV and 0.106 eV were determined for Tc, Tt, Ct and Cc, respectively.^{10,22} These barriers are relatively high to allow these conversions given the actual experimental conditions. Indeed, at present, gas phase PA molecules are seeded in a cooled molecular beam, with translational temperatures of T ~ 110 K as extracted from the KERD of the parent molecule (see Figure S1 of the supplementary material), although internal energies are measured higher (see further down), close to 280K due to the imperfect cooling of vibrations in the molecular beam. Nevertheless, we expect the dominant formation of the Tc isomer in the gas phase prior to interaction with light either in the single photon VUV ionisation or in the fs pump-probe experiments, excluding thus the contribution of the less stable isomers and tautomers of Tc in the present experiments. From now on, we will only consider the contribution from Tc most stable species.

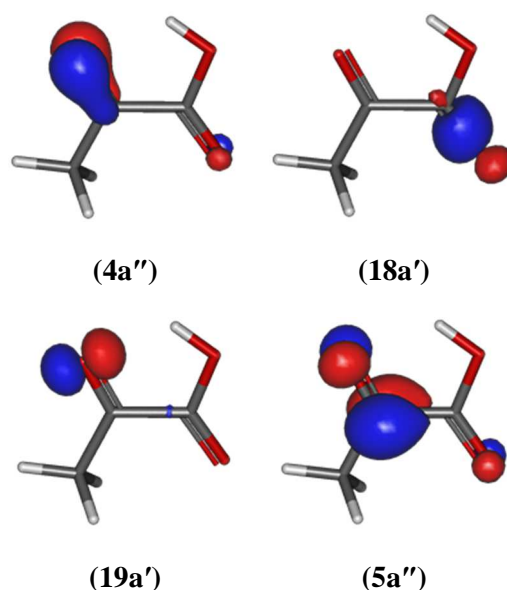


Figure 3: Outermost molecular orbitals of the Tc conformer of PA as computed at the CASSCF/aug-cc-pVDZ level.

Table 1: Vertical ionisation energies (VIE in eV) and dominant electronic configurations of the lowest-lying electronic states of Tc⁺ cation at the Tc ground state equilibrium geometry. These energies are given with respect to Tc (X¹A') energy at equilibrium.

State	Electronic configuration	VIE	
		This work ^{a)}	Ref. ^{43 b)}
D ₀ / X ² A'	(0.89) (4a'') ² (18a') ² (19a') ¹	10.628	10.42
D ₁ / 1 ² A''	(0.94) (4a'') ² (18a') ¹ (19a') ¹ (5a'') ¹	12.626	12.31
D ₂ / 2 ² A'	(0.86) (4a'') ² (18a') ¹ (19a') ²	12.725	12.42
D ₃ / 2 ² A''	(0.91) (4a'') ¹ (18a') ² (19a') ²	14.103	13.79

a) CASSCF/MRCI-F12/aug-cc-pVDZ calculations.

b) PES spectrum.

In the 9-12.5 eV energy range, the PES spectrum is composed of 2 large bands. ⁴³ McGlynn and Meeks tentatively assigned the first band to the PA⁺ + e⁻ ← PA + hν photoionisation transition, where both species are in their electronic ground states. In view of our calculations, we exclusively identify the contribution of the Tc isomer to the PES of McGlynn and Meeks in spite that it was measured using an effusive jet at room temperature. Table 1 shows that the ground state of Tc⁺ is obtained by removal of an electron from the HOMO, which corresponds to the 19a' oxygen lone pair of the ketone (Figure 3) as noticed by McGlynn and Meeks. Moreover, these authors assigned the second PES band to the population of the D₁ and D₂ states, whose vertical ionisation energies are computed at 12.626 eV and 12.725 eV (Table 1) at the CASSCF/MRCI-F12/aug-cc-pVDZ level, confirming thus such assignment. Nevertheless, our CASSCF/MRCI-F12 computations show that the electronic structure of D₁ (1²A'') and D₂ (2²A') cannot be accounted by simple considerations as proposed by McGlynn and Meeks based on CNDO. Indeed, inspection of the electronic configurations of these two cationic states reveals that their wavefunctions are dominantly described by the (4a'')²(18a')¹(19a')¹(5a'')¹ and (4a'')²(18a')¹(19a')² configurations in the Franck-Condon region accessed from Tc (X¹A'). Accordingly, the D₁ state is obtained by the ejection of an electron from the 18a' MO with simultaneous electron promotion from the 19a' MO into the vacant 5a'' MO. Since both states are close in energy, they form a conical intersection at which they interact vibronically. This results in the congestion of the spectrum consistent with a large band as observed experimentally and may complicate the dynamics of Tc⁺ ions at these energies.

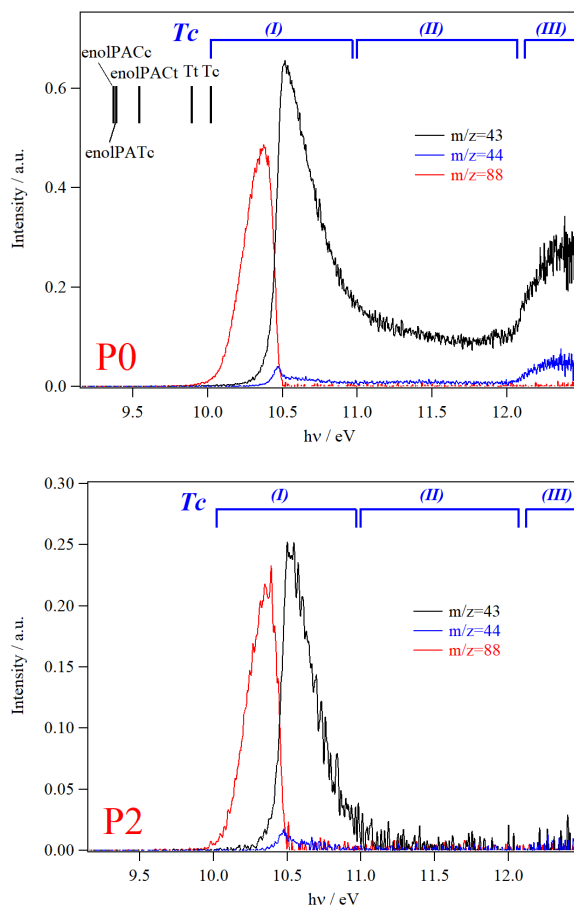


Figure 4: P0 (upper trace) and P2 (lower trace) spectra of Tc taking into account all photoelectrons with kinetic energies between 0 and 800 meV. The black vertical combs correspond to the adiabatic ionization energies of PA species as computed at the PBE0/aug-cc-pVDZ (opt) // (R)CCSD(T)-F12 /cc-pVTZ-F12 + Δ CV+ Δ SR+ Δ ZPVE (SP) level (Table 2). (I), (II) and (III) correspond to the three spectral regions discussed in the text.

Table 2: Adiabatic ionization energies (AIE in eV) of pyruvic acid species. Δ ZPE (in eV) is evaluated at the PBE0/aug-cc-pVDZ level using the corresponding anharmonic frequencies. Δ CV and Δ SR are for core valence and scalar relativistic effects. See Table S1-S3 for more details.

Method	Tc	Tt	enolPACc	enolPATc	enolPACt
PBE0/aug-cc-pVDZ (opt) // (R)CCSD(T)-F12 / cc-pVTZ-F12)	10.103	9.967	9.437	9.412	9.585
Δ CV	-0.0035	-0.0095	-0.0142	-0.0136	-0.0147
Δ SR	0.0004	0.000	-0.001	-0.001	-0.001
Δ ZPVE	-0.0729	-0.0635	-0.0324	-0.0234	-0.0300
PBE0 / aug-cc-pVDZ (opt) // (R)CCSD(T)-F12 /	10.027	9.894	9.389	9.374	9.539

cc-pVTZ-F12+ $\Delta CV + \Delta SR + \Delta ZPVE$ (SP)					
Exp.	10.031 ± 0.005 ^{a)} 10.1 ± 0.1 ^{b)}				

a) This work.

b) Ref. 43.

Figure 4 shows the P0 and P2 SPES spectra of PA as a function of the photon energy. These spectra were obtained by considering the photoelectrons having a kinetic energy between 0 and 800 meV in coincidence with the m/z 88, 44 and 43 mass peaks. On top of the PES spectrum, we reported the AIEs of PA species given in Table 2 as computed at a very high theoretical level (i.e. the PBE0/aug-cc-pVDZ (opt) // (R)CCSD(T)-F12 /cc-pVTZ-F12 + $\Delta CV + \Delta SR + \Delta ZPVE$ (SP) level). For instance, Table 2 shows that the computed AIEs for Tc, Tt, enolPACc, enolPATc and enolPACT are 10.027 eV, 9.894 eV, 9.389 eV, 9.374 eV and 9.539 eV, respectively. Nevertheless, these spectra reveal that no signal can be recorded for $h\nu < 10$ eV, where one may expect the population of the ground states of Tt⁺, enolPACc⁺, enolPATc⁺, enolPACT⁺ upon ionisation of the corresponding neutrals. In contrast, the SPES spectrum exhibits a large band starting at $h\nu \sim 10$ eV which is very close to the AIE computed for Tc. Therefore, this further confirms the unique contribution of Tc in the present experiments.

In Figure 4, we identify three regions: Region (*I*) extends from ~ 10 to ~ 11 eV corresponding to the population of the ground state (D_0) of Tc⁺; Region (*II*) is the Franck-Condon gap between the D_0 and D_1 states; and Region (*III*) for the D_1 & D_2 Tc⁺ states formation. When comparing the signals in each region in the P0 and P2 spectra, we noticed that solely Region (*I*) band is present in the P2 spectrum, while the two others vanish. This points out an evolution of the ionization process between Region (*I*) and (*II*). As Region (*II*) stands out of the Franck-Condon region, we consider this statement as a probe of autoionization processes dominating in Region (*II*). The same observation can be done in Region (*III*), although we cannot exclude the contribution of direct processes. For Region (*I*), direct processes are also dominating at threshold, but we cannot exclude autoionization processes.

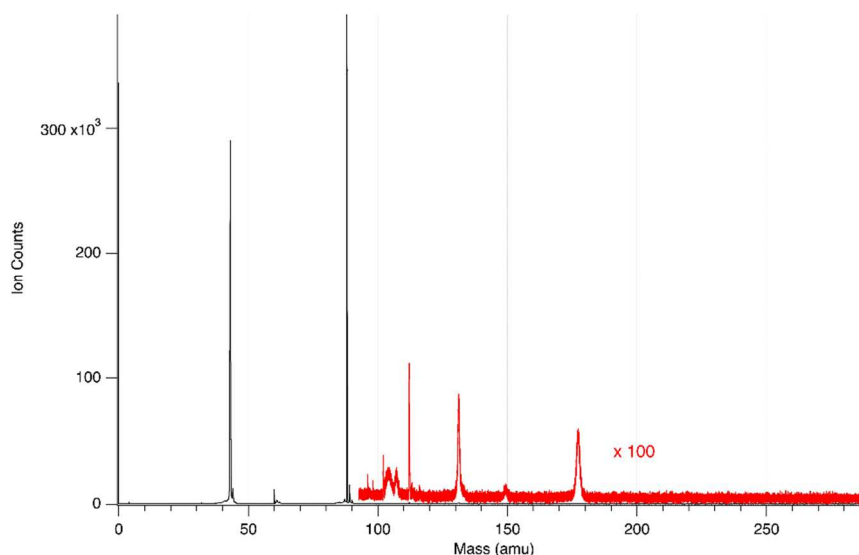


Figure 5: Integrated mass spectrum over the scan energy range (9.4 — 12.5 eV). The red part is magnified by 100. The peak at m/z 88 is the monomer parent. The peaks above this mass are due to ionised PA clusters or their fragments.

Figure 5 shows the TOF spectrum which presents two dominant peaks at m/z 88 and m/z 43 corresponding to Tc^+ parent and to its fragment. For $m/z < 88$, we observe two additional peaks at m/z 87 and 44. The analysis of the KERD reveals that the m/z 87 signal is due to dissociative ionization. Furthermore, the center of mass KER of m/z 87 is not compatible with a parent at m/z 88, so that it must come from fragmentation of a larger mass, such as the PA dimer (cf. Figure S1 of the supplementary material). However, m/z 44 is coming from Tc dissociative photoionisation. Figure 4 shows that the Tc^+ monomer (m/z 88) is stable for energies < 10.4 eV. For $h\nu > 10.4$ eV, it decomposes mainly to give a fragment of m/z 43 with contributions from m/z 44 signal. Although the decomposition of PA cations producing ionic fragment with m/z 44 was noticed in the early works by Lossing and Traeger⁴⁴ and by Terlouw et al.⁴⁵, the m/z 43 fragment is reported here for the first time, even though it dominates the mass spectrum above $h\nu=10.4$ eV. Interestingly, both ionic fragments appear at ~ 10.4 eV.

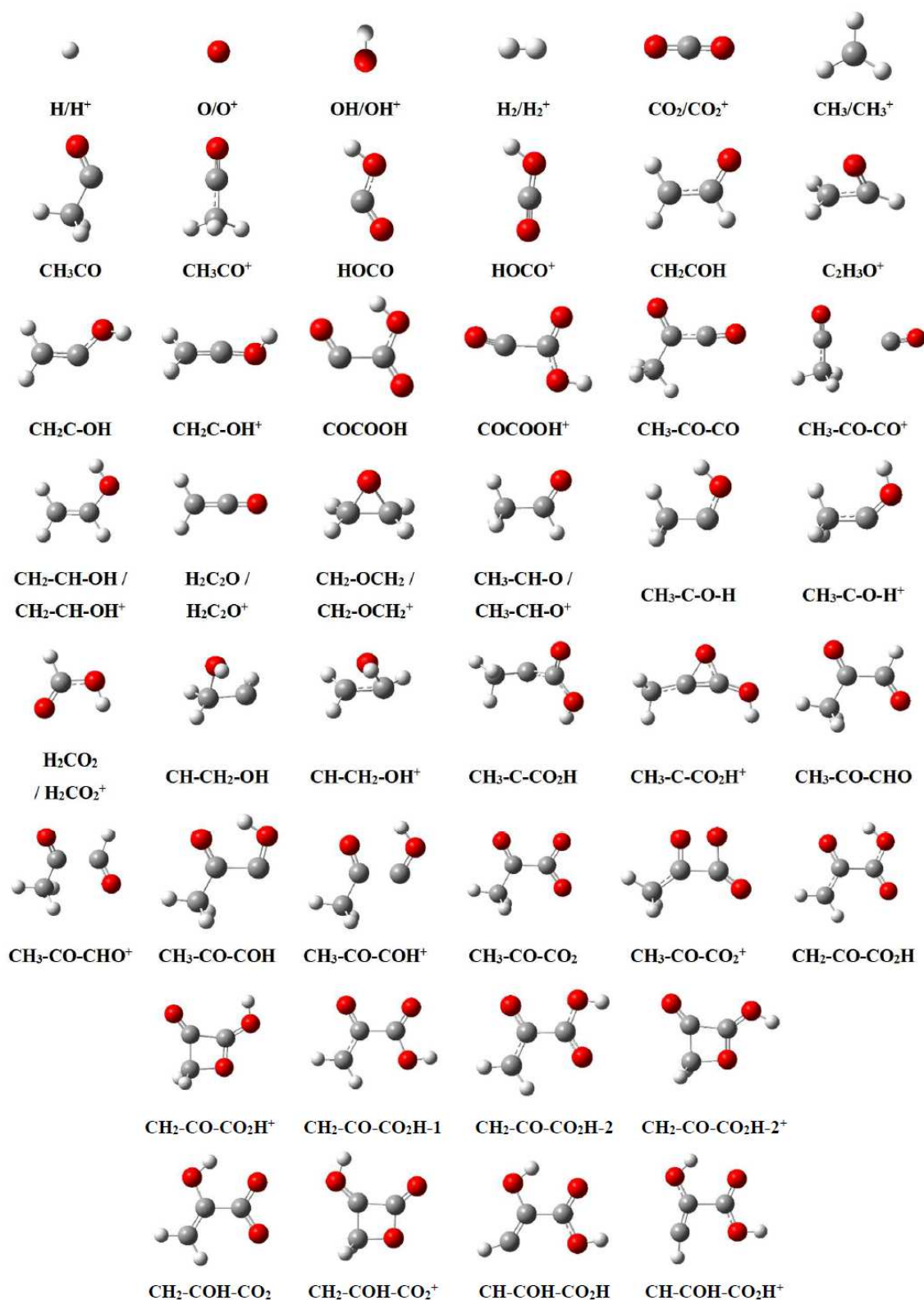


Figure 6: Equilibrium structures of neutral and ionic fragments considered in the present work. All species are taken in their electronic ground state. See Tables S4-S17 for more details.

Table 3: Appearance energies (AE in eV) of Tc⁺ fragments as computed at the PBE0/aug-cc-pVDZ (opt) // (R)CCSD(T)-F12 /cc-pVTZ-F12 + Δ CV+ Δ SR+ Δ ZPVE (SP) level of theory. These energies are given with respect to Tc ground state energy. See Tables S4-S17 for more details and Figure 6 for the fragment structures.

m/z	Fragments	AE
87	CH ₂ -CO-CO ₂ H ⁺ + H	12.484
87	CH ₂ -CO-CO ₂ H-2 ⁺ + H	12.490
87	CH ₂ -COH-CO ₂ ⁺ + H	13.107
87	CH-COH-CO ₂ H ⁺ + H	14.153
87	CH ₃ -CO-CO ₂ ⁺ + H	15.420
73	CH ₃ + COCOOH ⁺	11.813
72	CH ₃ -CO-CHO ⁺ + O	14.834
72	CH ₃ -CO-COH ⁺ + O	15.986
72	CH ₃ -C-CO ₂ H ⁺ + O	15.995
71	CH ₃ -CO-CO ⁺ + OH	11.249
46	H ₂ C ₂ O + H ₂ CO ₂ ⁺	12.395
45	CH ₃ CO + HOCO ⁺	11.550
45	CH ₂ COH + HOCO ⁺	11.838
45	CH ₂ C-OH + HOCO ⁺	12.870
44	CH ₂ -CH-OH ⁺ + CO ₂	9.450
44	CH ₃ -CH-O ⁺ + CO ₂	9.962
44	CH ₃ -C-O-H ⁺ + CO ₂	10.234
44	CH ₂ -OCH ₂ ⁺ + CO ₂	11.466
44	CH- CH ₂ -OH ⁺ + CO ₂	11.506
44	CH ₃ -CH-O + CO ₂ ⁺	13.506
44	CH ₂ -CH-OH + CO ₂ ⁺	13.963
44	H ₂ C ₂ O + CO ₂ ⁺ + H ₂	14.663
44	CH ₂ -OCH ₂ + CO ₂ ⁺	14.701
44	CH ₃ -C-O-H + CO ₂ ⁺	15.802
44	CH- CH ₂ -OH + CO ₂ ⁺	17.540
43	CH ₃ CO ⁺ + HOCO	10.411
43	C ₂ H ₃ O ⁺ + HOCO	12.809
43	CH ₂ C-OH ⁺ + HOCO	17.540
42	H ₂ C ₂ O ⁺ + CO ₂ + H ₂	10.431
42	H ₂ C ₂ O ⁺ + H ₂ CO ₂	10.660

17	$\text{CH}_3\text{-CO-CO} + \text{OH}^+$	17.625
16	$\text{CH}_3\text{-CO-CHO} + \text{O}^+$	18.752
16	$\text{CH}_3\text{-CO-COH} + \text{O}^+$	20.885
16	$\text{CH}_3\text{-C-CO}_2\text{H} + \text{O}^+$	21.342
15	$\text{CH}_3^+ + \text{COCO}_2\text{H}$	14.701
2	$\text{H}_2\text{C}_2\text{O} + \text{CO}_2 + \text{H}_2^+$	16.285
1	$\text{CH}_2\text{-CO-CO}_2\text{H} + \text{H}^+$	17.677
1	$\text{CH}_2\text{-CO-CO}_2\text{H-2} + \text{H}^+$	17.787
1	$\text{CH}_2\text{-CO-CO}_2\text{H-1} + \text{H}^+$	17.854
1	$\text{CH}_2\text{-COH-CO}_2 + \text{H}^+$	18.847
1	$\text{CH-COH-CO}_2\text{H} + \text{H}^+$	18.847
1	$\text{CH}_3\text{-CO-CO}_2 + \text{H}^+$	19.747

The precise appearance energy of the fragments has been extracted from the breakdown diagram displayed in Figure S2 of the supplementary material. The branching ratios of m/z 88 and 43 as a function of the internal energy, i.e. the photon energy when only threshold electrons are taken into account, can be modelled using a statistical approach that takes the initial thermal energy into account, while we assume that the dissociation reaction is fast within the experimental window of a few μsec . The internal energy distribution used by the model is constructed with the density of states obtained by direct counting from the calculated vibrational frequencies at the PBE0/aug-cc-pVDZ level. The resulting fit yields the overall vibrational temperature, at $T_{\text{vib}} = 270 \pm 20$ K, and the appearance energy at 0K, $AE_{0\text{K}} = 10.458 \pm 0.005$ eV.

For identification of these fragments we performed a search of all possible ionic fragments and their neutral counterparts at the PBE0/aug-cc-pVDZ level. The optimized molecular structures are displayed in Figure 6. They correspond to stable forms and they are taken in their ground electronic states. Note that for some species, several isomers/tautomers were identified. Afterwards, we carried out single point computations at the optimized geometries to deduce the appearance energies of these fragments at the PBE0/aug-cc-pVDZ (optg) // (R)CCSD(T)-F12 /cc-pVTZ-F12 + ΔCV + ΔSR + ΔZPVE (SP) level. The corresponding data are listed in Table 3, where these energies are given with respect to vibrationless Tc ground state energy.

For energies < 12.5 eV with respect to Tc (X^1A'), we locate at least 15 dissociation channels. They can be gathered in 8 groups corresponding to the losses of H, CH_3 , OH, $\text{H}_2\text{C}_2\text{O}$, CH_3O , CO_2 , HOCO, and $\text{H}_2+\text{CO}_2/\text{H}_2\text{CO}_2$ in conjunction with ionic fragments with m/z 87, 73, 71, 46, 45, 44, 43, 42. Figure 4 shows that the most favourable dissociation is for m/z 43. Computations reveal that this peak may be attributed to the formation of HOCO + CH_3CO^+ fragments that may be obtained via C2-C3 bond breaking (Figure 1). Indeed, we compute an AE of 10.411 eV for this channel, in very good agreement

with the measured $AE_{0K} = 10.458 \pm 0.005$ eV. In addition, a small contribution, around $h\nu = 10.4$ eV, is found for m/z 44. It is an ionic fragment associated with the decarboxylation upon dissociative photoionisation of Tc. The formation of CO_2 is a minor channel here contrary to the electronically excited neutral Tc decomposition as detailed in the Introduction. For the ionic structures, several possibilities are found, namely, $CH_2-CH-OH^+$, CH_3-CH-O^+ , $CH_3-C-O-H^+$ for which we compute AE of 9.450 eV, 9.962 eV and 10.234 eV, respectively, making the $CH_3-C-O-H^+$ ion the most likely structure in view of the experimental AE measured at 10.458 ± 0.005 eV. It is worth noting that many calculated channels are not seen experimentally, such as m/z 87 (loss of H, AE ~ 12.5), m/z 44 and those of m/z 73 (loss of CH_3 , AE = 11.813 eV), m/z 71 (loss of OH, AE = 11.249 eV), m/z 46 (loss of H_2C_2O , AE = 12.395 eV), m/z = 45 (loss of CH_3CO/CH_2COH , AE = 11.550 eV) and m/z 42 (loss of $H_2CO_2/CO_2 + H_2$, AE = 10.660/10.431 eV). In particular, we note the non-formation of the $HOCO^+$ cation by dissociative photoionization of Tc. The preferential and dominant formation of the m/z 43 fragment may explain the close to zero BRs for the other channels, which most likely are associated with large dissociation barriers or not favoured by the Tc dissociative photoionization mechanism in action (vide infra).

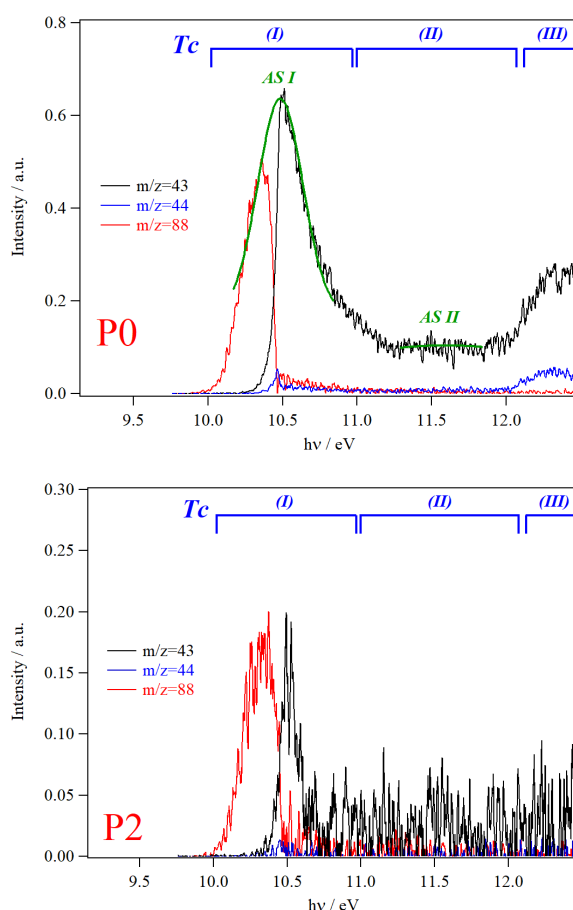


Figure 7: P0 (upper trace) and P2 (lower trace) spectra of PA taking into account all photoelectrons with kinetic energies between 0 and 50 meV. The green solid lines in the upper trace correspond to the

first (*AS I*) and second (*AS II*) autoionizing states discussed in the text. (*I*), (*II*) and (*III*) are the three spectral regions discussed in the text.

For better experimental spectral resolution, we present in Figure 7 the SPES spectra as obtained after considering all photoelectrons having kinetic energy smaller than 50 meV. These spectra exhibit some differences with those displayed in Figure 4. Also, a noticeable difference can be seen while comparing the P0 and P2 spectra in Figure 7. For instance, the P2 spectrum consists of 2 bands in Region (*I*) and almost zero signal in Region (*II*) and Region (*III*) whereas non-zero signals are recorded in these regions in spectrum P0. Again, this signature of an autoionisation process in action while photoionising Tc. Indeed, we highlight in Figure 7 the presence of two large bands, denoted as *AS I* and *AS II* at 10.48 eV and 11.60 eV, respectively. These states are also visible in the total ion yields (cf. Figure S3 of the supplementary material). We consider that these bands correspond to two short-lived autoionising states that contribute to the SPES signal. In Region (*I*), we first populate a highly excited neutral state (Tc^*) at 10.48 eV, that later ejects an electron. The second step is coupled with fragmentation, where we have $\text{Tc}^* \rightarrow \text{Tc}^+ + \text{e}^-$ for energies $< \text{AE}_{0\text{K}}$ and $\text{Tc}^* \rightarrow \text{HOCO} + \text{CH}_3\text{CO}^+ + \text{e}^-$ for energies $> \text{AE}_{0\text{K}}$. In the Franck-Condon gap (Region (*II*)), the short-lived electronically excited state at 11.60 eV is involved. It leads exclusively to $\text{HOCO} + \text{CH}_3\text{CO}^+ + \text{e}^-$. In Region (*III*), the D_1 and D_2 states of Tc^+ are formed, which dissociate to give m/z 43 and m/z 44 ionic fragments mainly via indirect dissociative photoionisation. For m/z 44 formation (i.e. decarboxylation upon ionisation), Figure 7 shows that CO_2 is ejected for energies close to $\text{AE}_{0\text{K}}$ and in Region (*III*) range. Nevertheless, the comparison of the corresponding P0 and P2 spectra reveals that the signal at $\sim \text{AE}_{0\text{K}}$ is present in both spectra, whereas it vanishes in P2 one in Region (*III*). Therefore, the direct and the indirect mechanisms are in action for $h\nu \sim \text{AE}_{0\text{K}}$. In Region (*III*), both D_1 & D_2 states are close in energy, they are coupled vibronically, leading to the congestion of the bands via vibronic couplings. Such couplings may also participate during the fragmentation, complicating even more the dynamics of electronically excited neutral Tc and Tc^+ ionic states at these energies. Simulations of such processes are challenging and out of the scope of the present investigations.

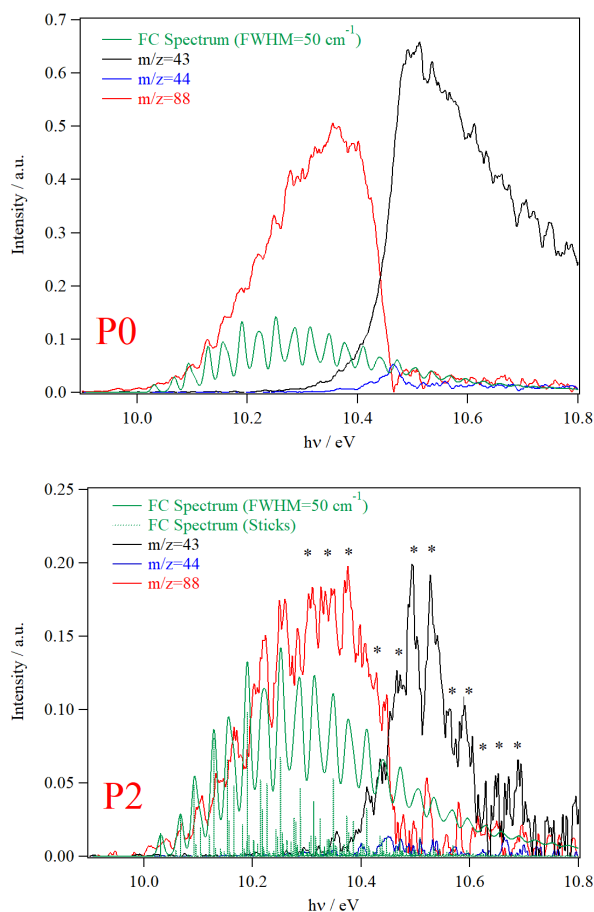


Figure 8: P0 (upper trace) and P2 (lower trace) spectra of PA in the photon energy covered by Region (I). We took into account all photoelectrons with kinetic energies between 0 and 50 meV. We give also the Franck-Condon simulated spectrum for the $\text{Tc}^+(\text{D}_0) + e^- \leftarrow \text{Tc}(\text{X}^1\text{A}') + h\nu$ photoionisation transition, where the first band is positioned in energy at the experimental AIE. We adopted a resolution of FWHM of 50 cm^{-1} ($=0.0062 \text{ eV}$) for the simulated spectrum. * corresponds to the enhanced autoionization peaks (see text for more details).

Table 4: Anharmonic frequencies (in cm^{-1}) of $\text{Tc}^+(\text{D}_0)$ as computed at the PBE0/aug-cc-pVDZ level of theory. We give also their symmetry, tentative assignment and atomic displacements. ν , stretching; δ , bending; γ , rocking; τ , torsion. s: symmetric; and as: asymmetric.

Mode	Sym.	Freq.	Assign.	Displ.	Mode	Sym.	Freq.	Assign.	Displ.
ν_1^+	a'	3457.6	$\nu(\text{OH})$		ν_{13}^+	a'	481.4	$\delta(\text{C2}=\text{C3})$	
ν_2^+	a'	3043.8	$\nu(\text{CH}_3)$ as		ν_{14}^+	a'	360.3	$\delta(\text{CCC})$	
ν_3^+	a'	2927.3	$\nu(\text{CH}_3)$ s		ν_{15}^+	a'	276.0	$\nu(\text{C2-C3})$	

ν_4^+	a'	1957.7	$\nu(\text{C3=O})$		ν_{16}^+	a'	219.8	$\delta(\text{CCO})$	
ν_5^+	a'	1868.8	$\nu(\text{C2=O})$		ν_{17}^+	a''	2982.3	$\nu(\text{CH}_3) \text{ as}$	
ν_6^+	a'	1374.6	$\delta(\text{CH}_3) \text{ as}$		ν_{18}^+	a''	1353.2	$\delta(\text{CH}_3) \text{ as}$	
ν_7^+	a'	1296.1	$\delta(\text{CH}_3) \text{ s}$		ν_{19}^+	a''	980.1	$\gamma(\text{C3=O})$	
ν_8^+	a'	1248.0	$\delta(\text{COH})$		ν_{20}^+	a''	647.9	$\gamma(\text{CH}_3)$	
ν_9^+	a'	1194.8	$\nu(\text{C-O})$		ν_{21}^+	a''	522.8	$\tau(\text{OH})$	
ν_{10}^+	a'	1009.1	$\nu(\text{C-C}) \text{ as}$		ν_{22}^+	a''	373.8	$\gamma(\text{C2=O})$	
ν_{11}^+	a'	914.5	$\gamma(\text{CH}_3)$		ν_{23}^+	a''	103.6	$\tau(\text{CH}_3)$	
ν_{12}^+	a'	583.8	$\nu(\text{C-C}) \text{ s}$		ν_{24}^+	a''	50.2	$\tau(\text{C-C})$	

Table 5: PBE0/aug-cc-pVDZ structural parameters (distances in Å, angles in degree) of Tc and Tc⁺ in their electronic ground states. See Figure 1 of the numbering of the atoms.

Parameter	Tc	Tc ⁺
C2=O1	1.215	1.173
C2-C3	1.543	1.784
C2-C4	1.488	1.474
C3=O5	1.203	1.181
C3-O6	1.329	1.281
O6-H7	0.977	0.977
C4-H8	1.093	1.095
C4-H9	1.099	1.101
C4-H10	1.099	1.101
C3-C2=O1	117.19	109.99
C4-C2=O1	125.46	136.27

O5=C3-C2	123.11	113.74
O6-C3=O5	124.54	132.93
H7-O6-C3	105.84	112.81
H8-C4-C2	110.26	108.99
H9-C4-C2	109.32	108.03
H10-C4-C2	109.32	108.03
H10-C4-C2=O1	122.30	122.07
H9-C4-C2=O1	-122.30	-122.07

Figure 8 displays an enlargement of the P0 and P2 spectra of Figure 7 in Region (I), where one can see that both spectra exhibit a long vibrational progression in the signals associated with m/z 88 (parent) and m/z 43 (CH_3CO^+ fragment). This progression is more pronounced in the P2 spectrum. For assignment, we estimated the anharmonic frequencies of Tc^+ (D_0) at the PBE0/aug-cc-pVDZ level (cf. Table 4). This ion has 24 vibrational modes: 16 a' and 8 a'' . Since both the neutral and the cation are planar in their electronic ground states, only the a' vibrational levels are populated upon single photon ionization of Tc, which are the levels of all a' vibrational modes, of all those having even quanta of a'' modes and to any multiple and combination modes of these vibrational states. Moreover, we computed the Franck-Condon spectrum corresponding to the Tc^+ (D_0) + $e^- \leftarrow \text{Tc}$ (X) + $h\nu$ transition. This spectrum has a relatively simple shape. This may be related to the slight structural differences between Tc (X^1A') and Tc^+ (D_0). Indeed, Table 5 reveals that the geometries of the cation and the neutral species mainly differ by the C2-C3 distance, which is lengthened from 1.543 Å to 1.784 Å upon ionisation. This also accompanied by more than 5° changes in the in-plane angles involving C2 and C3 atoms.

The simulated Franck-Condon spectrum is superposed to the experimental ones in Figure 8. Note that it corresponds solely to the direct ionisation process. The simulated spectrum consists of a long vibrational progression mostly due to the population of ν_{15}^+ vibrational bands and to the even quanta of ν_{24}^+ mode. Table 4 shows that both modes involve the CCC skeletal in Tc and they are thus strongly related to the C2-C3 bond breaking. Besides, the position of the first peak in the simulated spectrum corresponds to the AIE of Tc, which is determined $\text{AIE} = 10.031 \pm 0.005$ eV (Table 2).

The computed vibrational progression starts in the SPES relative to m/z 88 signal and continues in the m/z 43 one. Therefore, the vibrational levels of Tc^+ (D_0) located $> \text{AE}_{0\text{K}}$ are predissociated to lead to $\text{HOCO} + \text{CH}_3\text{O}^+$ products. Moreover, while the energy positions of the measured peaks and those of the simulated one are close, their relative intensities are quite different, in particular close and above $\text{AE}_{0\text{K}}$ (those marked by * in Figure 8). Since the Franck-Condon spectrum corresponds solely to direct processes, this highlights the contribution of resonant vibrational autoionization processes. The latter process enhances the production of $\text{HOCO} + \text{CH}_3\text{O}^+$ species.

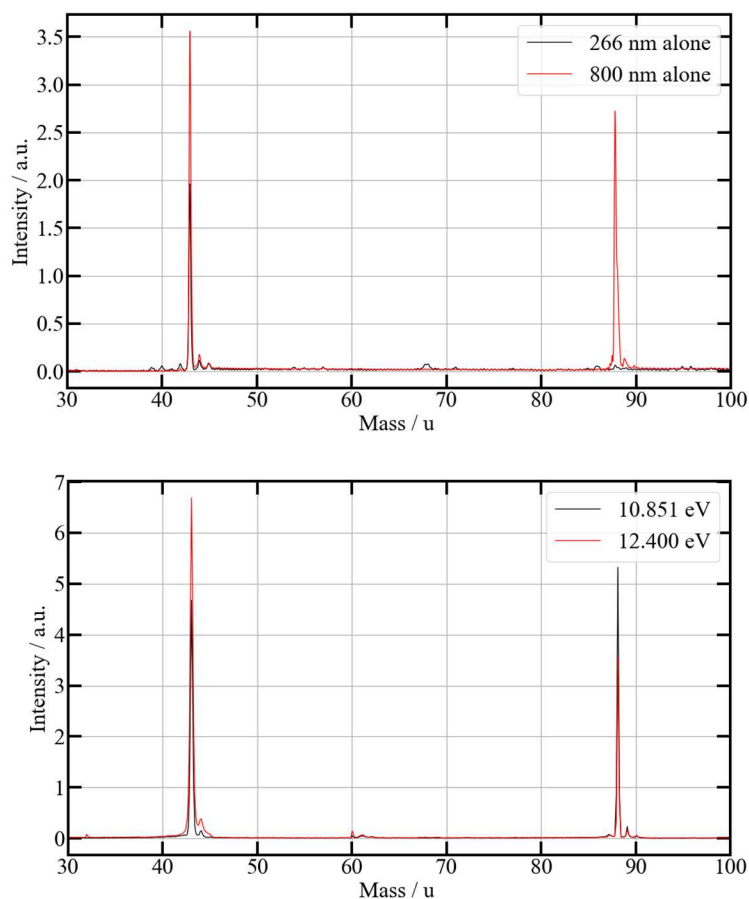


Figure 9: (top) One-color mass spectra for the multiphoton ionization of PA with the fs 266 nm (black) and 800 nm (red) (bottom). One-photon ionization mass spectra from the synchrotron experiment for energies of 10.85 eV and 12.40 eV.

Time-resolved relaxation dynamics of PA was investigated with a 266 nm pump and 800 nm acting as a multiphoton ionization probe. We first discuss the one-color mass spectra as reported on Figure 9. According to the AIE of Tc determined above, the minimal number of photons required to ionize Tc in the framework of a multiphoton ionization process is 3 and 7 for 266 nm and 800 nm respectively. In the first case, the total energy applied is about 13.95 eV whereas it is 10.85 eV in the last case. Multiphoton ionization with 266 nm leads also to the deposition of 1.5 eV more energy than considered for the synchrotron study presented above, and opens the way to multiple fragmentations. The parent peak is negligible compared to the main fragment that is m/z 43. m/z 44 remains a minor fragment.

Contrariwise, ionization with 800 nm leads to the presence of a strong parent signal, although the m/z 43 is dominating the mass spectrum. Indeed, as 800 nm is unable to ionize the molecule in a perturbative interaction, we observe here the result of the non-linear above threshold ionization process.⁸² Consequently, the energy absorbed by the molecule in the process is a multiple of the photon energy: 10.85 eV, 12.40 eV, 13.95 eV... depending whether respectively 7, 8 or 9 photons are absorbed. Also,

we compare in Figure 9 the mass spectra collected with the one photon ionization process at 10.85 and 12.4 eV (bottom) at the DESIRS beamline with the one issued from multiphoton ionization with 800 nm. No additional fragmentation channels are observed in the multiphoton scheme. Relative intensities show a clear contribution from higher energy ionization than the first 10.85 eV ionization process.

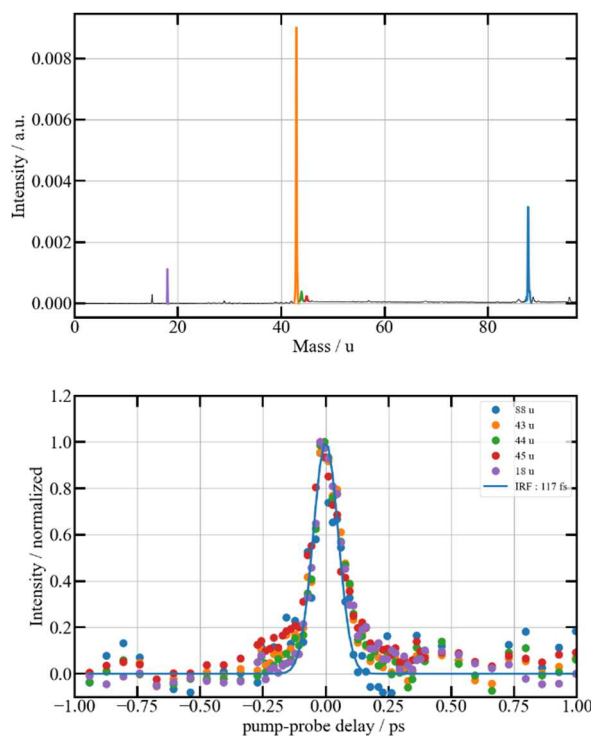


Figure 10: (Top) Mass spectrum collected at a pump-probe delay of 0 ps, that is at the temporal overlap of the two pulses. Mass peaks considered are highlighted in colour. (Bottom) Time-resolved evolution of the highlighted mass peaks with the corresponding colour. The blue line is the IRF of 117 fs.

For the time-resolved relaxation dynamics, the pump-alone and probe-alone signal discussed previously are subtracted from all the set of data to highlight the sole time-dependant signal. Since the AIE is 10.031 eV, the ionization scheme is $[1 + \geq 4^*]$. The total energy introduced in the molecule prior to ionization is also about 10.85 eV, 12.40 eV, 13.95 eV... for respectively 4, 5 or 6 probe photons that lead to the fragmentation of the molecule. The time-dependent mass spectra show the same fragments as observed in the one-photon experiment and single-color experiments (see Figure 10 (top)). Besides, one can notice the presence of low masses as 18 and 16 for water and oxygen atoms issued from the dissociation of residual dioxygen. As water does not absorb the pump laser, its mass peak is a benchmark for the measurement of the Instrumental Response Function (IRF). The mass peaks are highlighted with various colours; the same ones being used for plotting their time dependence on Figure 10 (Bottom). For negative times, that is the 800 nm pulse interacting with PA before the 266 nm pulse, some deviation to the water signal is observed. This is probably due to an intermediate resonance in Tc that is difficult to assign. For positive times, the time evolution shows a behaviour that is apparently the same for all

masses including water, which precludes the observation of a time-resolved process in Tc, using 266 nm (= 4.661 eV) as the pump laser. Such findings are consistent with the close to flat shape of the potential energy surfaces of the S_1 and T_1 states in the Franck-Condon region accessed from the ground state till reaching the region of S_0 - S_1 - T_1 potential crossings, which lead to the decarboxylation.³¹ Indeed, the wavepacket on the S_1 state obtained by 266 nm photon absorption from S_0 corresponds to the population to the highly excited vibrational states of S_1 i.e. those located in the Franck-Condon gap between the S_1 and S_2 states. It retains the same shape although it spans over a large range of nuclear configurations since only small potential barriers are found along the decarboxylation pathway from S_1 . Therefore, the subsequent multi photons ionisation leads to same products whatever the time delay between the pump and the probe. Let us notice that the one-photon absorption cross-section of Tc shows a minimum in the 266-290 nm region,⁸³ making the excitation to the S_2 state difficult. Future time-resolved experiments will target the S_0 - S_1 band at 320-370 nm.

IV. Conclusion

The present combined theoretical and experimental study treated the single photon VUV photoionisation and dissociative photoionisation of the most stable isomer of PA. We found that the electronic ground state lowest rovibrational levels of this isomer are stable, whereas the upper ones are predissociated leading mainly to the formation of the HOCO radical upon CC bond breaking. Interestingly, we show that the decarboxylation of the ground state of Tc^+ is a minor channel in contrast that it is a dominant process during the photolysis of electronically excited states of Tc. We also performed fs-based time-resolved mass spectra with 266 nm excitation and 800 nm multiphoton probe of this isomer. No appreciable dynamics at short timescales is observed due to unfavourable population of the rovibrational levels located in the S_1 - S_2 Franck-Condon gap. In summary, our combined theoretical and experimental approach allowed fully picturing the processes occurring after Tc – UV/VUV light interactions. In particular, we showed the couplings between the ion vibrational modes and the dissociative channels in the vicinity of the CO_2 loss ionic fragmentation threshold, as recently observed in the benzophenone cation fragmentation dynamics.⁸⁴

Author Contributions

M.J., A.B. and M.H. performed the computations. M.J., L.B., D.C., G.A.G., L.P. and M.H. performed the experiments. L.P. and M.H. designed the work. M.H. wrote the first version of the manuscript. All authors contributed in editing the final version.

Conflicts of interest

There are no conflicts to declare.

Acknowledgements

M.J. thanks the Tunisian Ministry for Higher Education and Research for a fellowship for the preparation of this work. We are indebted to the general technical staff of Synchrotron Soleil for running the facility under proposal # 20210040. We would like also to thank J.-F. Gil and L. Nahon for their help.

Supporting information: We give the full set of theoretical data, including optimized equilibrium structures of the neutral and ionic pyruvic acid and its fragments and of their energetics. We give also the KERD spectra, the breakdown diagram showing the branching ratio of parent (m/z 88) and fragment (m/z 43) ions and their ion yields as a function of photon energy.

REFERENCES

- ¹ S. I. Fox, Human Physiology (12th ed.) McGraw-Hill, 2011
- ² M. O. Andreae, R. W. Talbot and S. M. Li, Atmospheric measurements of pyruvic and formic acid, *Journal of Geophysical Research: Atmospheres*, 1987, **92**, 6635–6641, DOI: 10.1029/JD092ID06P06635.
- ³ B. Nozière, M. Kalberer, M. Claeys, J. Allan, B. D’Anna, S. Decesari, E. Finessi, M. Glasius, I. Grgić, J. F. Hamilton, T. Hoffmann, Y. Iinuma, M. Jaoui, A. Kahnt, C. J. Kampf, I. Kourtchev, W. Maenhaut, N. Marsden, S. Saarikoski, J. Schnelle-Kreis, J. D. Surratt, S. Szidat, R. Szmigielski and A. Wisthaler, The Molecular Identification of Organic Compounds in the Atmosphere: State of the Art and Challenges, *Chemical Reviews*, 2015, **115**, 3919–3983, DOI: 10.1021/CR5003485.
- ⁴ D. J. Jacob and S. C. Wofsy, Photochemistry of biogenic emissions over the Amazon forest, *Journal of Geophysical Research: Atmospheres*, 1988, **93**, 1477–1486, DOI: 10.1029/JD093ID02P01477.
- ⁵ S. Yu, . Role of organic acids (formic, acetic, pyruvic and oxalic) in the formation of cloud condensation nuclei (CCN): a review, *Atmospheric Research*, 2000, **53**, 185–217, DOI: 10.1016/S0169-8095(00)00037-5.
- ⁶ A. Mellouki, T. J. Wallington and J. Chen, Atmospheric chemistry of oxygenated volatile organic compounds: impacts on air quality and climate, *Chemical reviews*, 2015, **115**, 3984–4014, DOI: 10.1021/CR500549N.
- ⁷ R. W. Talbot, M. O. Andreae, H. Berresheim, D. J. Jacob and K. M. Beecher, Sources and sinks of formic, acetic, and pyruvic acids over central Amazonia: 2. Wet season, *Journal of Geophysical Research: Atmospheres*, 1990, **95**, 16799–16811, DOI: 10.1029/JD095ID10P16799.
- ⁸ M. I. Stefan and J. R. Bolton, Reinvestigation of the Acetone Degradation Mechanism in Dilute Aqueous Solution by the UV/H₂O₂ Process, *Environmental Science and Technology*, 1999, **33**, 870–873, DOI: 10.1021/ES9808548.
- ⁹ N. F. Kleimeier, A. K. Eckhardt, P. R. Schreiner and R. I. Kaiser, Interstellar Formation of Biorelevant Pyruvic Acid (CH₃COCOOH), *Chem*, 2020, **6**, 3385–3395 DOI: 10.1016/J.CHEMPR.2020.10.003.
- ¹⁰ Z. Kisiel, L. Pszczółkowski, E. Białkowska-Jaworska and S. B. Charnley, The millimeter wave rotational spectrum of pyruvic acid, *Journal of Molecular Spectroscopy*, 2007, **241**, 220–229, DOI: 10.1016/J.JMS.2006.12.011.
- ¹¹ C. E. Kaluza, A. Bauder and H. H. Günthard, The microwave spectrum of pyruvic acid, *Chemical Physics Letters*, 1973, **22**, 454–457, DOI: 10.1016/0009-2614(73)87006-X.
- ¹² K. M. Marstokk and H. Møllendal, Microwave spectrum, conformation, barrier to internal rotation and dipole moment of pyruvic acid, *Journal of Molecular Structure*, 1974, **20**, 257–267 DOI: 10.1016/0022-2860(74)85094-5.

-
- ¹³ C. E. Dyllick-Brenzinger, A. Bauder and H. H. Günthard, The substitution structure, barrier to internal rotation, and low frequency vibrations of pyruvic acid, *Chemical Physics*, 1977, **23**, 195–206, DOI: 10.1016/0301-0104(77)89002-2.
- ¹⁴ R. Meyer, A. Bauder, R. Meyer and A. Bauder, Torsional coupling in pyruvic acid, *Journal of Molecular Spectroscopy*, 1982, **94**, 136–149, DOI: 10.1016/0022-2852(82)90300-9.
- ¹⁵ H. Hollenstein, F. Akermann and H. H. Günthard, Vibrational analysis of pyruvic acid and D-, ¹³C- and ¹⁸O-labelled species: Matrix spectra, assignments, valence force field and normal coordinate analysis, *Spectrochimica Acta Part A: Molecular Spectroscopy*, 1978, **34**, 1041–1063, DOI: 10.1016/0584-8539(78)80127-5.
- ¹⁶ I. Reva, C. M. Nunes, M. Biczysko and R. Fausto, Conformational Switching in Pyruvic Acid Isolated in Ar and N₂ Matrixes: Spectroscopic Analysis, Anharmonic Simulation, and Tunneling, *Journal of Physical Chemistry A*, 2014, **119**, 2614–2627, DOI: 10.1021/JP509578C.
- ¹⁷ K. Takahashi, K. L. Plath, R. T. Skodje and V. Vaida, Dynamics of vibrational overtone excited pyruvic acid in the gas phase: Line broadening through hydrogen-atom chattering, *Journal of Physical Chemistry A*, 2008, **112**, 7321–7331, DOI: 10.1021/JP803225C.
- ¹⁸ K. L. Plath, K. Takahashi, R. T. Skodje and V. Vaida, Fundamental and Overtone Vibrational Spectra of Gas-Phase Pyruvic Acid, *Journal of Physical Chemistry A*, 2009, **113**, 7294–7303, DOI: 10.1021/JP810687T.
- ¹⁹ E. D. Raczyńska, K. Duczmal and M. Darowska, Experimental (FT-IR) and theoretical (DFT-IR) studies of keto–enol tautomerism in pyruvic acid, *Vibrational Spectroscopy*, 2005, **39**, 37–45, DOI: 10.1016/J.VIBSPEC.2004.10.006.
- ²⁰ P. Tarakeshwar and S. Manogaran, An ab initio study of pyruvic acid, *Journal of Molecular Structure: THEOCHEM*, 1998, **430**, 51–56, DOI: 10.1016/S0166-1280(98)90215-9.
- ²¹ V. Barone, M. Biczysko, J. Bloino, P. Cimino, E. Penocchio and C. Puzzarini, CC/DFT Route toward Accurate Structures and Spectroscopic Features for Observed and Elusive Conformers of Flexible Molecules: Pyruvic Acid as a Case Study, *Journal of Chemical Theory and Computation*, 2015, **11**, 4342–4363, DOI: 10.1021/ACS.JCTC.5B00580.
- ²² M. L. Senent and S. Dalbouha, Large Amplitude Motions of Pyruvic Acid (CH₃-CO-COOH), *Molecules*, 2021, **26**, 4269–4282, DOI: 10.3390/MOLECULES26144269.
- ²³ R. Kakkar, M. Pathak and N. P. Radhika, A DFT study of the structures of pyruvic acid isomers and their decarboxylation, *Organic & Biomolecular Chemistry*, 2006, **4**, 886–895, DOI: 10.1039/B516355B.
- ²⁴ S. L. Blair, A. E. Reed Harris, B. N. Frandsen, H. G. Kjaergaard, E. Pangui, M. Cazaunau, J. F. Doussin and V. Vaida, Conformer-Specific Photolysis of Pyruvic Acid and the Effect of Water, *Journal of Physical Chemistry A*, 2020, **124**, 1240–1252, DOI: 10.1021/ACS.JPCA.9B10613.
- ²⁵ G. Buemi, DFT study of the hydrogen bond strength and IR spectra of formic, oxalic, glyoxylic and pyruvic acids in vacuum, acetone and water solution, *Journal of Physical Organic Chemistry*, 2009, **22**, 933–947, DOI: 10.1002/POC.1543.

-
- ²⁶ Z. Zhou, D. Du and A. Fu, Structures and vibrational frequencies of pyruvic acid: density functional theory study, *Vibrational Spectroscopy*, 2000, **23**, 181–186, DOI: 10.1016/S0924-2031(00)00061-8.
- ²⁷ S. Yamamoto and R. A. Back, The photolysis and thermal decomposition of pyruvic acid in the gas phase, *Canadian Journal of Chemistry*, 2011, **63**, 549–554, DOI: 10.1139/V85-089.
- ²⁸ A. Horowitz, R. Meller and G. K. Moortgat, The UV–VIS absorption cross sections of the α -dicarbonyl compounds: pyruvic acid, biacetyl and glyoxal, *Journal of Photochemistry and Photobiology A: Chemistry*, 2001, **146**, 19–27, DOI: 10.1016/S1010-6030(01)00601-3.
- ²⁹ A. Prlj, E. Marsili, L. Hutton, D. Hollas, D. Shchepanovska, D. R. Glowacki, P. Slavíček and B. F. E. Curchod, Calculating Photoabsorption Cross-Sections for Atmospheric Volatile Organic Compounds, *ACS Earth and Space Chemistry*, 2021, **6**, 207–217, DOI: 10.1021/ACSEARTHSPACECHEM.1C00355.
- ³⁰ S. Sutradhar, B. R. Samanta, R. Fernando and H. Reisler, Spectroscopy and Two-Photon Dissociation of Jet-Cooled Pyruvic Acid, *Journal of Physical Chemistry A*, 2019, **123**, 5906–5917, DOI: 10.1021/ACS.JPCA.9B04166.
- ³¹ X. P. Chang, Q. Fang and G. Cui, Mechanistic photodecarboxylation of pyruvic acid: Excited-state proton transfer and three-state intersection, *The Journal of Chemical Physics*, 2014, **141**, 154311, DOI: 10.1063/1.4898085.
- ³² A. E. Reed Harris, A. Pajunoja, M. Cazaunau, A. Gratien, E. Pangui, A. Monod, E. C. Griffith, A. Virtanen, J. F. Doussin and V. Vaida, Multiphase Photochemistry of Pyruvic Acid under Atmospheric Conditions, *Journal of Physical Chemistry A*, 2017, **121**, 3327–3339, DOI: 10.1021/ACS.JPCA.7B01107.
- ³³ K. J. Kappes, A. M. Deal, M. F. Jaspersen, S. L. Blair, J. F. Doussin, M. Cazaunau, E. Pangui, B. N. Hopper, M. S. Johnson and V. Vaida, Chemistry and Photochemistry of Pyruvic Acid at the Air-Water Interface, *Journal of Physical Chemistry A*, 2021, **125**, 1036–1049, DOI: 10.1021/ACS.JPCA.0C09096.
- ³⁴ M. D. P. Barquilla and M. L. Mayes, A computational study of the gas-phase pyruvic acid decomposition: Potential energy surfaces, temporal dependence, and rates, *AIP Advances*, 2021, **11**, 015243, DOI: 10.1063/5.0036649.
- ³⁵ B. R. Samanta, R. Fernando, D. Rösch, H. Reisler and D. L. Osborn, Primary photodissociation mechanisms of pyruvic acid on S1: observation of methylhydroxycarbene and its chemical reaction in the gas phase, *Physical Chemistry Chemical Physics*, 2021, **23**, 4107–4119, DOI: 10.1039/D0CP06424F.
- ³⁶ P. G. Eger, L. Vereecken, R. Sander, J. Schuladen, N. Sobanski, H. Fischer, E. Karu, J. Williams, V. Vakkari, T. Petäjä, J. Lelieveld, A. Pozzer and J. N. Crowley, Impact of pyruvic acid photolysis on acetaldehyde and peroxy radical formation in the boreal forest: Theoretical calculations and model results, *Atmospheric Chemistry and Physics*, 2021, **21**, 14333–14349, DOI: 10.5194/ACP-21-14333-2021.

-
- ³⁷ G. da Silva, Decomposition of Pyruvic Acid on the Ground-State Potential Energy Surface, *Journal of Physical Chemistry A*, 2016, **120**, 276–283, DOI: 10.1021/ACS.JPCA.5B10078.
- ³⁸ A. E. Reed Harris, M. Cazaunau, A. Gratien, E. Pangui, J. F. Doussin and V. Vaida, Atmospheric Simulation Chamber Studies of the Gas-Phase Photolysis of Pyruvic Acid, *Journal of Physical Chemistry A*, 2017, **121**, 8348–8358, DOI: 10.1021/ACS.JPCA.7B05139.
- ³⁹ A. E. Reed Harris, J. F. Doussin, B. K. Carpenter and V. Vaida, Gas-Phase Photolysis of Pyruvic Acid: The Effect of Pressure on Reaction Rates and Products, *Journal of Physical Chemistry A*, 2016, **120**, 10123–10133, DOI: 10.1021/ACS.JPCA.6B09058.
- ⁴⁰ A. Mellouki and Y. Mu, On the atmospheric degradation of pyruvic acid in the gas phase, *Journal of Photochemistry and Photobiology A: Chemistry*, 2003, **157**, 295–300, DOI: 10.1016/S1010-6030(03)00070-4.
- ⁴¹ R. D. Saini, S. Dhanya, D. K. Maity, H. P. Upadhyaya, A. Kumar and P. D. Naik, Dynamics of OH formation in photodissociation of pyruvic acid at 193 nm, *The Journal of Chemical Physics*, 2003, **118**, 10093, DOI: 10.1063/1.1572133.
- ⁴² B. R. Samanta, R. Fernando, D. Rösch, H. Reisler and D. L. Osborn, Looking at the bigger picture: Identifying the photoproducts of pyruvic acid at 193 nm, *The Journal of Chemical Physics*, 2020, **153**, 074307, DOI: 10.1063/5.0018582.
- ⁴³ S. P. McGlynn and J. L. Meeks, Photoelectron spectra of carbonyls: Acetaldehyde, acetamide, biacetyl, pyruvic acid, methyl pyruvate and pyruvamide, *Journal of Electron Spectroscopy and Related Phenomena*, 1975, **6**, 269–279, DOI: 10.1016/0368-2048(75)80037-5.
- ⁴⁴ F. P. Lossing and J. C. Traeger, Free radicals by mass spectrometry XLVI. Heats of formation of C₅H₇ and C₅H₉ radicals and cations, *International Journal of Mass Spectrometry and Ion Physics*, 1976, **19**, 9–22, DOI: 10.1016/0020-7381(76)83002-1.
- ⁴⁵ J. K. Terlouw, J. Wezenberg, P. C. Burgers and J. L. Holmes, New, stable isomers of [C₂H₄O]⁺, and [C₂H₄O₂]⁺, the radical cations [CH₃COH]⁺ and [CH₃OCOH]⁺, *Journal of the Chemical Society, Chemical Communications*, 1983, **0**, 1121–1123, DOI: 10.1039/C39830001121.
- ⁴⁶ J. L. Holmes, F. P. Lossing and P. M. Mayer, Heats of formation of oxygen-containing organic free radicals from appearance energy measurements, *Journal of the American Chemical Society*, 2002, **113**, 9723–9728, DOI: 10.1021/JA00026A002.
- ⁴⁷ K. Grygoryeva, M. Ončák, A. Pysanenko and M. Fárník, Pyruvic acid proton and hydrogen transfer reactions in clusters, *Physical Chemistry Chemical Physics*, 2019, **21**, 8221–8227, DOI: 10.1039/C8CP07008C.
- ⁴⁸ DESIRS, French national synchrotron facility, <https://www.synchrotron-soleil.fr/en/beamlines/desirs>.
- ⁴⁹ M. Hochlaf, Advances in spectroscopy and dynamics of small and medium sized molecules and clusters, *Physical Chemistry Chemical Physics*, 2017, **19**, 21236–21261, DOI: 10.1039/C7CP01980G.
- ⁵⁰ A. Bellili, Z. Gouid, M. C. Gazeau, Y. Bénilan, N. Fray, J. C. Guillemin, M. Hochlaf and M. Schwell, Single photon ionization of methyl isocyanide and the subsequent unimolecular decomposition of its

cation: experiment and theory, *Physical Chemistry Chemical Physics*, 2019, **21**, 26017–26026, DOI: 10.1039/C9CP04310A.

⁵¹ I. Derbali, H. R. Hrodmarsson, M. Schwell, Y. Bénilan, L. Poisson, M. Hochlaf, M. E. Alikhani, J. C. Guillemin and E. L. Zins, Unimolecular decomposition of methyl ketene and its dimer in the gas phase: theory and experiment, *Physical Chemistry Chemical Physics*, 2020, **22**, 20394–20408, DOI: 10.1039/D0CP03921G.

⁵² I. Derbali, H. R. Hrodmarsson, Z. Gouid, M. Schwell, M. C. Gazeau, J. C. Guillemin, M. Hochlaf, M. E. Alikhani and E. L. Zins, Photoionization and dissociative photoionization of propynal in the gas phase: theory and experiment, *Physical Chemistry Chemical Physics*, 2019, **21**, 14053–14062, DOI: 10.1039/C8CP06751A.

⁵³ L. Nahon, N. de Oliveira, G. A. Garcia, J. F. Gil, B. Pilette, O. Marcouillé, B. Lagarde and F. Polack, DESIRS: a state-of-the-art VUV beamline featuring high resolution and variable polarization for spectroscopy and dichroism at SOLEIL, *urn:issn:0909-0495*, 2012, **19**, 508–520, DOI: 10.1107/S0909049512010588.

⁵⁴ G. A. Garcia, B. K. Cunha De Miranda, M. Tia, S. Daly and L. Nahon, DELICIOUS III: A multipurpose double imaging particle coincidence spectrometer for gas phase vacuum ultraviolet photodynamics studies, *Review of Scientific Instruments*, 2013, **84**, 053112, DOI: 10.1063/1.4807751.

⁵⁵ A. T. J. B. Eppink and D. H. Parker, Velocity map imaging of ions and electrons using electrostatic lenses: Application in photoelectron and photofragment ion imaging of molecular oxygen, *Review of Scientific Instruments*, 1998, **68**, 3477, DOI: 10.1063/1.1148310.

⁵⁶ J. C. Poully, J. P. Schermann, N. Nieuwjaer, F. Lecomte, G. Grégoire, C. Desfrancois, G. A. Garcia, L. Nahon, D. Nandi, L. Poisson and M. Hochlaf, Photoionization of 2-pyridone and 2-hydroxypyridine, *Physical Chemistry Chemical Physics*, 2010, **12**, 3566–3572, DOI: 10.1039/B923630A.

⁵⁷ M. Briant, L. Poisson, M. Hochlaf, P. de Pujo, M. A. Gaveau and B. Soep, Ar 2 photoelectron spectroscopy mediated by autoionizing states, *Physical Review Letters*, 2012, **109**, 193401, DOI: 10.1103/PHYSREVLETT.109.193401.

⁵⁸ G. A. Garcia, H. Soldi-Lose and L. Nahon, A versatile electron-ion coincidence spectrometer for photoelectron momentum imaging and threshold spectroscopy on mass selected ions using synchrotron radiation, *Review of Scientific Instruments*, 2009, **80**, 023102, DOI: 10.1063/1.3079331.

⁵⁹ Anja Röder. Excited-State Dynamics in Open-Shell Molecules. Theoretical and/or physical chemistry. Université Paris-Saclay; Julius-Maximilians-Universität (Wurtzbourg, Allemagne), 2017. English. (NNT : 2017SACLS099). (tel-01576556)

⁶⁰ J. M. Mestdagh and L. Poisson, Excited State Dynamics of Isolated 6- and 8-Hydroxyquinoline Molecules, *ChemPhysChem*, 2020, **21**, 2605–2613, DOI: 10.1002/CPHC.202000626.

⁶¹ C. Adamo and V. Barone, Toward reliable density functional methods without adjustable parameters: The PBE0 model, *The Journal of Chemical Physics*, 1999, **110**, 6158, DOI: 10.1063/1.478522.

⁶² M. J. Frisch et al. Gaussian 16, revision A.02, Gaussian, Inc., Wallingford, CT, 2016.

-
- ⁶³ T. H. Dunning, Gaussian basis sets for use in correlated molecular calculations. I. The atoms boron through neon and hydrogen, *The Journal of Chemical Physics*, 1998, **90**, 1007, DOI: 10.1063/1.456153.
- ⁶⁴ R. A. Kendall, T. H. Dunning and R. J. Harrison, Electron affinities of the first-row atoms revisited. Systematic basis sets and wave functions, *The Journal of Chemical Physics*, 1998, **96**, 6796, DOI: 10.1063/1.462569.
- ⁶⁵ MOLPRO version 2015 is a set of ab initio programs. Werner H.-J. et al., 2015. More details are available at <http://www.molpro.net>
- ⁶⁶ T. B. Adler, H. J. Werner and F. R. Manby, Local explicitly correlated second-order perturbation theory for the accurate treatment of large molecules, *The Journal of Chemical Physics*, 2009, **130**, 054106, DOI: 10.1063/1.3040174.
- ⁶⁷ T. B. Adler and H. J. Werner, Local explicitly correlated coupled-cluster methods: Efficient removal of the basis set incompleteness and domain errors, *The Journal of Chemical Physics*, 2009, **130**, 241101, DOI: 10.1063/1.3160675.
- ⁶⁸ T. B. Adler, G. Knizia, H.-J. Werner, A simple and efficient CCSD(T)-F12 approximation. *The Journal of Chemical Physics*, 2007, **127**, 221106, <https://doi.org/10.1063/1.2817618>
- ⁶⁹ G. Knizia, T. B. Adler and H. J. Werner, Simplified CCSD(T)-F12 methods: Theory and benchmarks, *The Journal of Chemical Physics*, 2009, **130**, 054104, DOI: 10.1063/1.3054300.
- ⁷⁰ K. A. Peterson, T. B. Adler and H. J. Werner, Systematically convergent basis sets for explicitly correlated wavefunctions: The atoms H, He, B–Ne, and Al–Ar, *The Journal of Chemical Physics*, 2008, **128**, 084102, DOI: 10.1063/1.2831537.
- ⁷¹ K. E. Yousaf and K. A. Peterson, Optimized auxiliary basis sets for explicitly correlated methods, *The Journal of Chemical Physics*, 2008, **129**, 184108, DOI: 10.1063/1.3009271.
- ⁷² G. Rauhut, G. Knizia and H. J. Werner, Accurate calculation of vibrational frequencies using explicitly correlated coupled-cluster theory, *The Journal of Chemical Physics*, 2009, **130**, 054105, DOI: 10.1063/1.3070236.
- ⁷³ K. A. Peterson and T. H. Dunning, Accurate correlation consistent basis sets for molecular core-valence correlation effects: The second row atoms Al–Ar, and the first row atoms B–Ne revisited, *Journal of Chemical Physics*, 2002, **117**, 10548–10560, DOI: 10.1063/1.1520138.
- ⁷⁴ M. Douglas and N. M. Kroll, Quantum electrodynamical corrections to the fine structure of helium, *Annals of Physics*, 1974, **82**, 89–155, DOI: 10.1016/0003-4916(74)90333-9.
- ⁷⁵ G. Jansen and B. A. Hess, Revision of the Douglas-Kroll transformation, *Physical Review A*, 1989, **39**, 6016, DOI: 10.1103/PhysRevA.39.6016.
- ⁷⁶ W. A. de Jong, R. J. Harrison and D. A. Dixon, Parallel Douglas–Kroll energy and gradients in NWChem: Estimating scalar relativistic effects using Douglas–Kroll contracted basis sets, *The Journal of Chemical Physics*, 2000, **114**, 48, DOI: 10.1063/1.1329891.
- ⁷⁷ P. J. Knowles and H. J. Werner, An efficient second-order MCSCF method for long configuration expansions, *Chemical Physics Letters*, 1985, **115**, 259–267, DOI: 10.1016/0009-2614(85)80025-7.

-
- ⁷⁸ H. J. Werner and P. J. Knowles, A second order multiconfiguration SCF procedure with optimum convergence, *The Journal of Chemical Physics*, 1998, **82**, 5053, DOI: 10.1063/1.448627.
- ⁷⁹ T. Shiozaki, G. Knizia and H. J. Werner, Explicitly correlated multireference configuration interaction: MRCI-F12, *The Journal of Chemical Physics*, 2011, **134**, 034113, DOI: 10.1063/1.3528720.
- ⁸⁰ T. Shiozaki and H. J. Werner, Explicitly correlated multireference configuration interaction with multiple reference functions: Avoided crossings and conical intersections, *The Journal of Chemical Physics*, 2011, **134**, 184104, DOI: 10.1063/1.3587632.
- ⁸¹ T. Shiozaki and H. J. Werner, Multireference explicitly correlated F12 theories, *Molecular Physics*, 2013, **111**, 607–630, DOI: 10.1080/00268976.2013.779393.
- ⁸² P. Agostini, F. Fabre, G. Mainfray, G. Petite and N. K. Rahman, Free-Free Transitions Following Six-Photon Ionization of Xenon Atoms, *Physical Review Letters*, 1979, **42**, 1127, DOI: 10.1103/PhysRevLett.42.1127.
- ⁸³ A. Horowitz, R. Meller and G. K. Moortgat, The UV–VIS absorption cross sections of the α -dicarbonyl compounds: pyruvic acid, biacetyl and glyoxal. *Journal of Photochemistry and Photobiology A: Chemistry*, *Journal of Photochemistry and Photobiology A: Chemistry*, 2001, **146**, 19–27, DOI: 10.1016/S1010-6030(01)00601-3.
- ⁸⁴ Z. Gouid, A. Röder, B. K. Cunha De Miranda, M. A. Gaveau, M. Briant, B. Soep, J. M. Mestdagh, M. Hochlaf and L. Poisson, Energetics and ionization dynamics of two diarylketone molecules: benzophenone and fluorenone, *Physical Chemistry Chemical Physics*, 2019, **21**, 14453–14464, DOI: 10.1039/C9CP02385B.